

Interactions between a Developing Mesoscale Convective System and Its Environment. Part II: Numerical Simulation

JASON E. NACHAMKIN* AND WILLIAM R. COTTON

Department of Atmospheric Science, Colorado State University, Fort Collins, Colorado

(Manuscript received 17 March 1999, in final form 24 June 1999)

ABSTRACT

The 19 July 1993 mesoscale convective system (MCS), discussed in Part I, was simulated using the Regional Atmospheric Modeling System (RAMS). The model was initialized with variable physiographic and atmospheric data with the goal of reproducing the convective system and its four-dimensional environment. Four telescopically nested, moving grids allowed for horizontal grid spacings down to 1.67 km on the cloud resolving grid. Comparisons with the analysis show that the propagation, evolution, and structure of this MCS were well simulated.

The simulation is used to further investigate the interactions between this MCS and its surrounding environment. In Part I, the Doppler-derived winds indicated that upshear (westward) propagating gravity waves left upper-tropospheric front-to-rear and midtropospheric rear-to-front flow perturbations in their wake. A similar flow structure developed in the simulated MCS, and unlike the Doppler results, the low-frequency waves that produced it were resolved in the data. In the simulation, much of the convectively generated temperature and momentum perturbations propagated westward with the waves, leaving a warm wake in the clear air trailing the system. Although the gravity waves traveled rearward, the perturbation flow in their wake was not strong enough to reverse the upper-tropospheric storm-relative winds. Thus, most of the anvil condensate advected ahead of the convective line.

As the MCS encountered the low-level jet, the midtropospheric upward mass flux increased, but gravity wave motions became less detectable. The upper-tropospheric anvil pushed westward into the strong flow as the system expanded into a characteristically oval shape. Temperature and momentum perturbations propagated rearward along with the anvil in a disturbance that resembled an advective outflow. Unlike the gravity waves, this disturbance became almost stationary with respect to the ground, and it retained its continuity through the rest of the simulation. Vertical cross sections indicate that a large slab of convectively processed air had detrained into the upper troposphere. Prior to this event, much of the warm temperature anomalies generated within the convective towers either remained in the updrafts, or propagated outward with the gravity waves. Early on, individual updrafts were relatively erect and although condensate did detrain eastward in the forward anvil, the temperature anomalies did not propagate with it. In contrast, convective updrafts associated with the expanding oval anvil disturbance were more continuous, and they tilted strongly westward with height.

1. Introduction

Maddox (1980) defined the mesoscale convective complex (MCC) as a mesoscale convective system (MCS) that maintained a large, contiguous cold cloud shield for at least 6 h. The MCC criteria were chosen to isolate those systems that were relatively round, with minor axis/major axis ≥ 0.7 at the time of maximum extent. However, Anderson and Arritt (1998) noted that elongated systems that did not meet the eccentricity criteria could also be as large and persistent as an MCC.

Additionally, Nachamkin et al. (1994), McAnelly et al. (1997), and Knupp et al. (1998) have observed significant mesoscale circulations in smaller systems that at best marginally met the MCC size criteria.

At what point does a growing MCS produce a large, mature, long-lasting atmospheric disturbance? The term *large* or *mature* often implies that the circulations have reached a scale that is on the order of the entire cloud shield. In Nachamkin et al. (2000, hereafter Part I), we used the term “upscale growth” after McAnelly et al. (1997) to describe the processes by which the convective cluster reaches a state of mesoscale organization. Once a system has grown upscale, a significant component of the circulation may be projected onto an inertially balanced state, such as geostrophic (Cotton and Anthes 1989), or nonlinear (Olsson and Cotton 1997), balance. Just how *large* a system needs to be in order to do this depends mainly on latitude, local vorticity, and the speed at which the latent heating is communi-

* Current affiliation: Naval Research Laboratory, Monterey, California.

Corresponding author address: Dr. Jason Nachamkin, Naval Research Laboratory, 7 Grace Hopper Ave., Monterey, CA 13943.
E-mail: nachamkin@nrlmry.navy.mil

cated to the surroundings. These parameters are related through the Rossby radius of deformation:

$$\lambda_R = \frac{NH}{(\zeta + f)^{0.5}(2VR^{-1} + f)^{0.5}}, \quad (1)$$

where N is the Brunt–Väisälä frequency, H is the scale height of the circulation, ζ is the vertical component of the relative vorticity, f is the Coriolis parameter, V is the tangential wind around the disturbance, and R is the radius of curvature. By the time a transient disturbance, such as a gravity wave, travels a distance λ_R from its source, a significant amount of its energy has been projected onto the balanced circulation. If the energy release is maintained for a sufficient period, the wind field adjusts to perturbations in the mass field and a mesoscale atmospheric disturbance, such as a vortex, develops (Bosart and Sanders 1981; Bartels and Maddox 1991; Johnson and Bartels 1992; Fritsch et al. 1994). In a composite of MCCs taken over the United States, Cotton et al. (1989) found that the typical value of λ_R for most midlatitude systems was ~ 300 km. This was slightly smaller than the average cloud shield radius of ~ 320 km.

When considering balance from the standpoint of the Rossby radius, the definition of the MCS must be carefully considered. What is the best demarcation between the system and the surrounding environment? If most of the convective heating spreads outward in the form of deep gravity waves as described by Bretherton and Smolarkiewicz (1989), Nicholls et al. (1991), Pandya et al. (1993), and Mapes (1993), then the mid- and upper-tropospheric temperature anomalies will not necessarily coincide with the cloud shield. Mapes (1993), Johnson et al. (1995), Pandya and Durran (1996), McAnelly et al. (1997), as well as the results in Part I of this work, have shown that MCS-generated disturbances can extend well outside the anvil.

Mounting evidence suggests that MCS-generated latent heating expands outward in many different ways. Indeed, even among gravity waves a continuum of disturbances exists, all spreading outward at varying speeds. Nicholls et al. (1991) and Mapes (1993) noted that much of the gravity wave energy was partitioned into two fundamental modes, one associated with deep a tropospheric convective heating ($n1$) profile, and the other a more stratiform profile with upper-tropospheric heating and lower-tropospheric cooling ($n2$). The $n1$ and $n2$ modes were found to propagate at 30 m s^{-1} and 15 m s^{-1} , respectively. Since these waves spread outward from convection regardless of its size, some component of the heating will spread to the scale of the Rossby radius in even the more modest convective systems. In addition to the gravity waves, latent heating processes within the contiguous stratiform precipitation region are also important to the development of a mesoscale disturbance. LeMone (1983) showed that a midtropospheric hydrostatic low forms due to heating within the highly

tilted convective towers. Brown (1979) and Smull and Houze (1987) pointed out that the combination of general latent heating within the stratiform anvil and cooling at low levels also combine to lower the midtropospheric pressure and in turn draw in midlevel rear inflow. The relative contributions of the gravity waves and the stratiform region to the mesoscale disturbance remains unknown. Since gravity waves are generated by latent heating, the two are not mutually exclusive.

Some evidence suggests that the convection responsible for MCCs and their qualitatively similar counterparts is fundamentally different from that of weaker MCSs. Maddox (1980), McAnelly and Cotton (1986), and Velasco and Fritsch (1987) all note that most MCC cloud shields grow explosively early in their life cycle, rapidly attaining an oval shape. Maddox (1980) and Velasco and Fritsch (1987) also noted that intense midlatitude systems often exhibited very uniform cold cloud shields in which the individual cells were difficult to distinguish. Velasco and Fritsch (1987) observed that although weaker, low-latitude systems met the satellite criteria, the cloud shields contained many irregularities and qualitatively resembled an agglomeration of discrete thunderstorms. Laing and Fritsch (1997) suggested that the strong early growth may be the distinguishing factor between the intense, symmetric systems and the weaker agglomerations. However, the reasons for this distinction were not readily apparent.

With so many processes occurring simultaneously, defining the point at which genesis or upscale development takes place is quite difficult. As we shall see, different types of mesoscale circulations will develop depending upon the forcing. In some cases, these may be superimposed upon strong ambient shear and thus be partially hidden in the storm-relative frame (Part I). This paper is a continuation of the analysis in Part I in which strong evidence of gravity wave propagation was found in the dual-Doppler data. In this paper, the wave structure as well as the structure of the spreading convective anvil are examined in greater detail through use of a high-resolution numerical simulation. The extent to which the model reproduced the 19 July MCS is discussed, and from there the results are used to help explain how the observed characteristics developed.

2. Model description and setup

Starting from a variable initialization, the Regional Atmospheric Modeling System (RAMS; Pielke et al. 1992) was run with the nonhydrostatic, compressible set of equations set in σ_z coordinates. The philosophy was to simulate the heterogeneous environment in as much detail as possible for direct comparison with the observations. To achieve this, four telescopically nested, three-dimensional grids were used (Fig. 1) as summarized in Table 1. Two-way interactive nesting (Clark and Farley 1984; Clark and Hall 1991) was used, and Klemp and Wilhelmson (1978a,b) radiative conditions were ap-

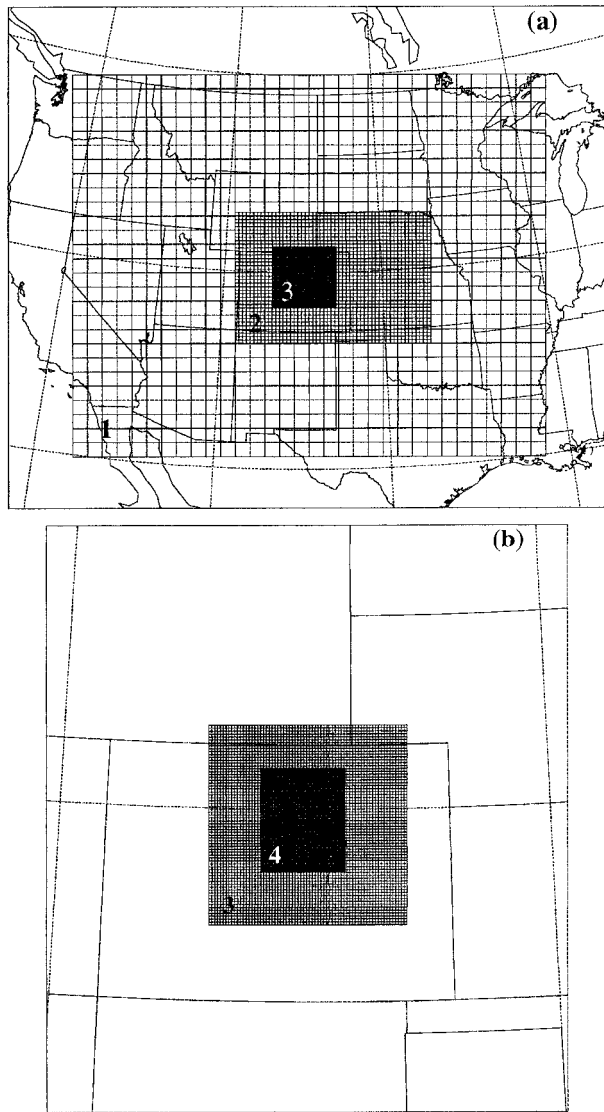


FIG. 1. Grid configuration for the variably initialized primitive equation simulation. Grids 1, 2, and 3 are shown in (a) and grids 3 and 4 are shown in (b).

plied to all of the lateral boundaries. Grids 1 and 2 were stationary through the simulation, while grids 3 and 4 could move to follow convection.

The topography was initialized from the United States Geological Survey 30-s (~900 m) dataset. Since grids 3 and 4 could move, topography was interpolated onto these grids from grid 2. Although this effectively limited the topographical grid spacing to 20 km, the basic features of the Rocky Mountains, the Palmer Divide, and the Cheyenne Ridge were still well resolved (Fig. 2). Soil moisture was initialized with rainfall observations from the previous three months using the antecedent precipitation index method of Wetzel and Chang (1988). Due to the lack of reliable data in the mountains, soil moisture values above 2400 m were set to $0.18 \text{ m}^3 \text{ m}^{-3}$.

TABLE 1. Summary of the grid configuration used in the simulation.

19 Jul case	
Grid 1	Grid spacing: 80 km 33 × 28 points Time step: 90 s
Grid 2	Grid spacing: 20 km 54 × 38 points Time step: 45 s
Grid 3	Grid spacing: 5 km 70 × 70 points Time step: 15 s
Grid 4	Grid spacing: 1.67 km 89 × 110 points Time step: 5 s
Vertical grid spacing	Starts at 100 m, stretched to 800 m at upper levels; model top at 19.5 km
Soil layers	Seven points at depths of 0 (surface), 3, 6, 9, 18, 35, and 50 cm

Without this, low default soil moisture resulted in uncharacteristically strong upslope flow. All soil moisture values were subsequently smoothed using a nine-point linear filter. The variable vegetation data were initialized from a 1° (111 km) dataset based on Loveland et al. (1991). The soil and vegetative cover were parameterized using the Tremback and Kessler (1985) and Avissar and Mahrer (1988) schemes. Surface fluxes were calculated based on Louis (1979). The Smagorinsky (1963) scheme with dependencies on the Brunt-Väisälä frequency (Hill 1974) and the Richardson number (Lilly

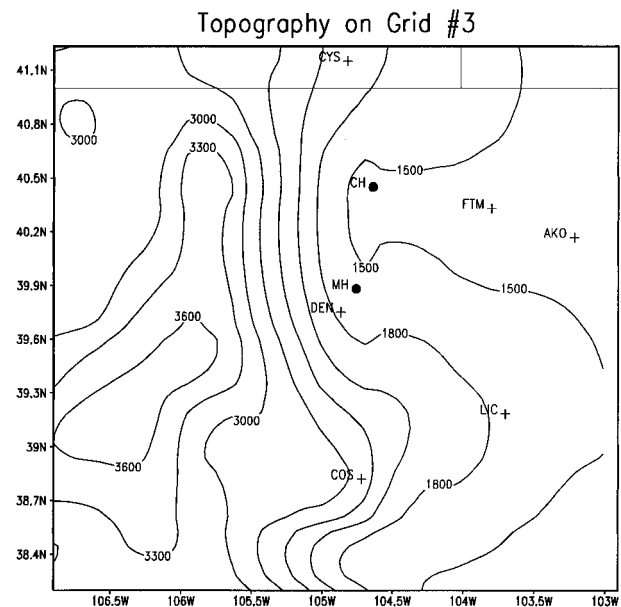


FIG. 2. Model topography on grid 3. Contours are labeled every 300 m.

1962) was used for the diffusion. The microphysics were parameterized with the bulk one-moment scheme of Walko et al. (1995). The mixing ratios of vapor, cloud water, rain, snow, pristine ice, aggregates, graupel, and hail were all predicted based on a gamma size distribution. Atmospheric scattering and absorption of shortwave and longwave radiation were parameterized with the Mahrer and Pielke (1977) scheme. Although the effects of condensed liquid and ice are neglected by the Mahrer–Pielke scheme, the early stages of the MCS were the focus of this simulation. The convective dynamics likely dominated over radiation at this time.

Initial atmospheric data consisted of the 1200 UTC¹ 19 July 1993 Forecast Systems Lab Mesoscale Analysis and Prediction System (MAPS)² (Benjamin et al. 1991) analyses, as well as the standard National Weather Service surface (NWS) and upper-air observations. The MAPS data included aircraft reports as well as mesonet and profiler data interpolated to a hybrid sigma-isentropic grid with 60-km horizontal spacing. Additional analyses at 0000 and 1200 20 July acted as upper and lateral boundary conditions for grid 1. The boundaries were adjusted to the observations using Davies (1983) nudging at the five outermost horizontal and the six uppermost vertical grid points.

The integration was started at 1200 19 July 1993 and a 15-h forecast was generated. Grids 1–3 were started at the time of initiation, while grid 4 was spawned 6 h into the run. To conserve computer resources, the microphysics were limited to the prediction of vapor and cloud water until grid 4 was spawned. Since the first simulated storms did not develop on grid 4 until 1900, the lack of parameterized precipitation did not affect development.

The model configuration allowed convective storms to form on simulated convergence zones as opposed to user-imposed warm bubbles. Convection was explicitly resolved on grid 4 in that the dominant motions within each thunderstorm were simulated without the use of convective parameterization. Interactions between convection and its environment could thus be studied without the restrictions of such parameterizations.

3. Comparisons with the observations

a. Synoptic overview

While comparisons with the observations will be done throughout this work, the overview here provides a general evaluation of the model performance. The 12-h forecast valid at 0000 20 July on grid 1 at 500 hPa (Fig. 3) can be compared to the observations in Fig. 2a of Part I.³ Most simulated heights and wind speeds were

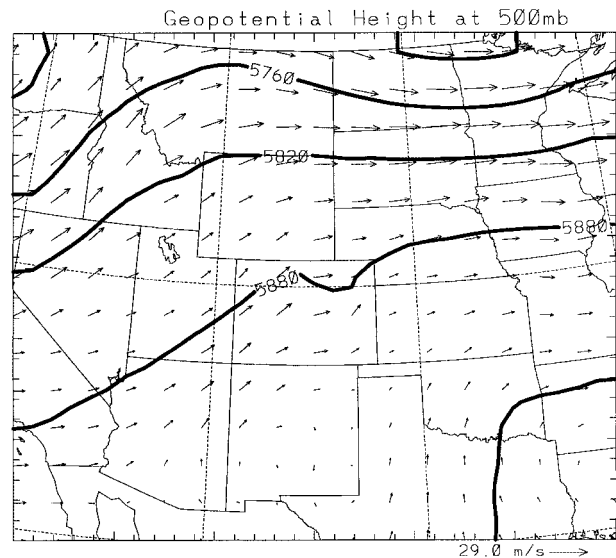


FIG. 3. The 12-h forecast on grid 1 valid at 0000 20 Jul. Geopotential height at 500 hPa is contoured at 60-m intervals, and wind vectors are plotted to the scale at the lower right.

within 2 dam and 5 m s^{-1} of the observations, respectively. The biggest differences occurred near the U.S.–Canadian border, where model heights were up to 6 dam lower than the NWS observations. This is a little surprising given the Davies nudging; however, the MAPS heights (not shown) were lower in this region than those from the soundings alone. This region was about 1000 km from the MCS, and any detrimental effects were assumed to be minimal. The simulated shortwave over Colorado was in response to convection. The coarse resolution of the sounding data prevented any observations of any feature at this scale. Similar analyses showed good agreement between the model and the observations at the 850-, 700-, and 200-hPa levels.

Near the surface (Fig. 4), simulated temperatures were within 5°C of the observations (Fig. 3 of Part I) in most areas. The exceptions were in the mountainous terrain in north-central Colorado, where the simulated temperatures were consistently too low. Part of the error was due to terrain smoothing. Most of the reporting stations were located in valleys, which in the model topography were up to 300 m above their true elevation. The increased soil moisture also reduced the temperatures at the highest elevations. The strength of the upslope flow in eastern Colorado at 0000 was slightly overpredicted despite the increased soil moisture. Simulated speeds at the first model level above the ground [$\sigma_z = 49 \text{ m}$ above ground level (AGL)] were 6 to 10 m s^{-1} , whereas most surface observations were closer to 5 m s^{-1} . Wind direction, however, was well simulated. The model also captured the weak north–south temperature gradient across the plains. The strongest simulated warm advection, located over northeastern Colorado and northwestern Kansas, corresponded to the track of the

¹ All times UTC.

² This model was a precursor to the Rapid Update Cycle.

³ To save space, the reader is referred to Part I for the majority of the observations.

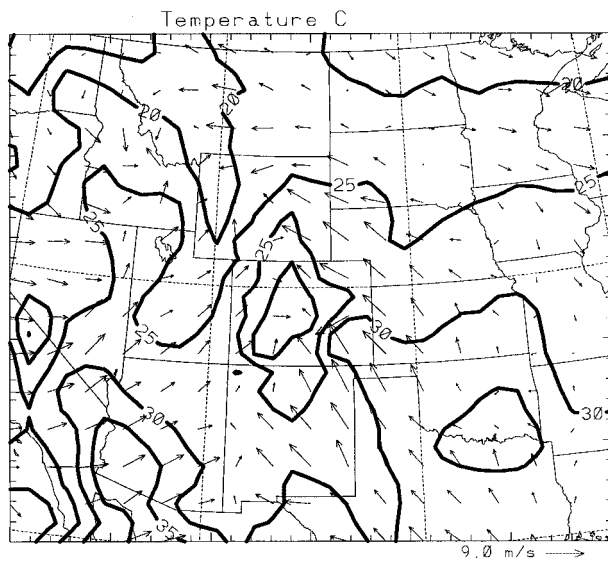


FIG. 4. The 12-h forecast on grid 1 valid at 0000 20 Jul. Temperature at the lowest σ_z level (49 m AGL) is contoured at 5°C intervals, and wind vectors are plotted to the scale at the lower right.

MCS. Maddox (1983) showed that large nocturnal convective systems often propagate along these regions of strong warm advection.

b. MCS overview

Total condensate, consisting of rain and hail, at the lowest model sigma level (Fig. 5) can be compared to the radar reflectivity (Fig. 6 of Part I) as another measure of the model performance. Several aspects of the storm-scale evolution indicate that the system was well simulated. Once the initial cells moved off the mountains, a north–south-oriented line developed along a simulated convergence zone southeast of Denver. Nachamkin (1998) noted that the structure of this convergence was very similar to the that observed in the mesonet.

By 2200 (Fig. 5a), strong low-level outflow developed, and the simulated line even took on the bowed appearance observed on radar (Fig. 6b of Part I). System placement was quite accurate, although the timing was about half an hour faster than observed. Simulated outflow wind speeds reached 34 m s^{-1} , while 27 m s^{-1} winds were measured. After 2200, the simulated convective line propagation was more discrete than observed. As a result, the simulated line slowed down and did not reach Colorado–Kansas boarder until 0300. The observed line reached this position at 0145. Despite the timing discrepancies, the general storm track and linear convective configuration were well represented.

As the system intercepted the intensifying low-level jet after 2330, strong updrafts repeatedly developed at the southwestern edge of the line. Many of these formed in the same area, just southeast of Limon, Colorado (LIC in Figs. 5c,d; Fig. 6d of Part I), and slowly moved

northeastward. The length of the convective line was extended toward the southwest through this back-building process (Bluestein and Jain 1985). Simulated system-total volumetric rainfall rates quadrupled between 0000 and 0130, while radar-derived rates quadrupled between 2300 and 0000. These corresponded with the rapid growth of both the observed and simulated cloud shields.

The system evolution can be summarized more quantitatively by the MCS-average divergence and MCS-integrated vertical mass flux profiles (Fig. 6). For comparisons with the Doppler-derived values, the model velocity data on grid 4 were only sampled at grid points where the combined mixing ratio of precipitation-sized particles (snow, aggregates, rain, graupel, and hail) was greater than 0.1 g kg^{-1} . This covered most of the active precipitating cloud much like the radar would.

After 1930, the general shape and magnitude of the divergence profile changed little through the entire simulation despite the pulsating convection. Convergence extended through most of the midtroposphere with a maximum near 5 km, while divergence dominated the upper and lower troposphere. The general pattern compares well with the Doppler observations in Part I (Fig. 25a). The magnitude of the simulated divergence and convergence maxima were somewhat larger than observed, but the relative values were similar at most levels. As mentioned in Part I, lower- and upper-tropospheric data were unrepresentative due to the lack of precipitation particles. Only the strongest overshooting tops were sampled above 12 km, while mainly precipitating downdrafts were sampled below 4 km. To get a better estimate of the average area-wide divergence, additional profiles were calculated over all of grid 4 without the conditional sampling. These depicted convergence through the entire troposphere below 8 km, but the maximum convergence was still near 6 km. Divergence extended between 8 and 15 km, and the maximum values were between 12 and 13 km. This corresponded closely to the simulated tropopause.

The structure and temporal evolution of the simulated mass flux field (Fig. 6b) between 2200 and 0000 is also similar to the Doppler observations (Fig. 26a of Part I). Through the period, the mid- and upper troposphere were dominated by net upward vertical mass flux, with maximum values near 8 km. Downdrafts dominated both profiles below 4 km. A temporal midtropospheric mass flux maximum occurred at 2130 in the model and at 2227 in the observations. In both cases, this coincided with the intensification of convection in a preexisting boundary layer convergence zone southeast of Denver. The simulated storm moved off the mountains and into this feature more rapidly, thus accounting for the earlier pulse in the mass flux. As convection moved east of the convergence zone, upward mass flux decreased in both cases.

After 2300, the observed midtropospheric upward mass flux began increasing but was decreasing again by

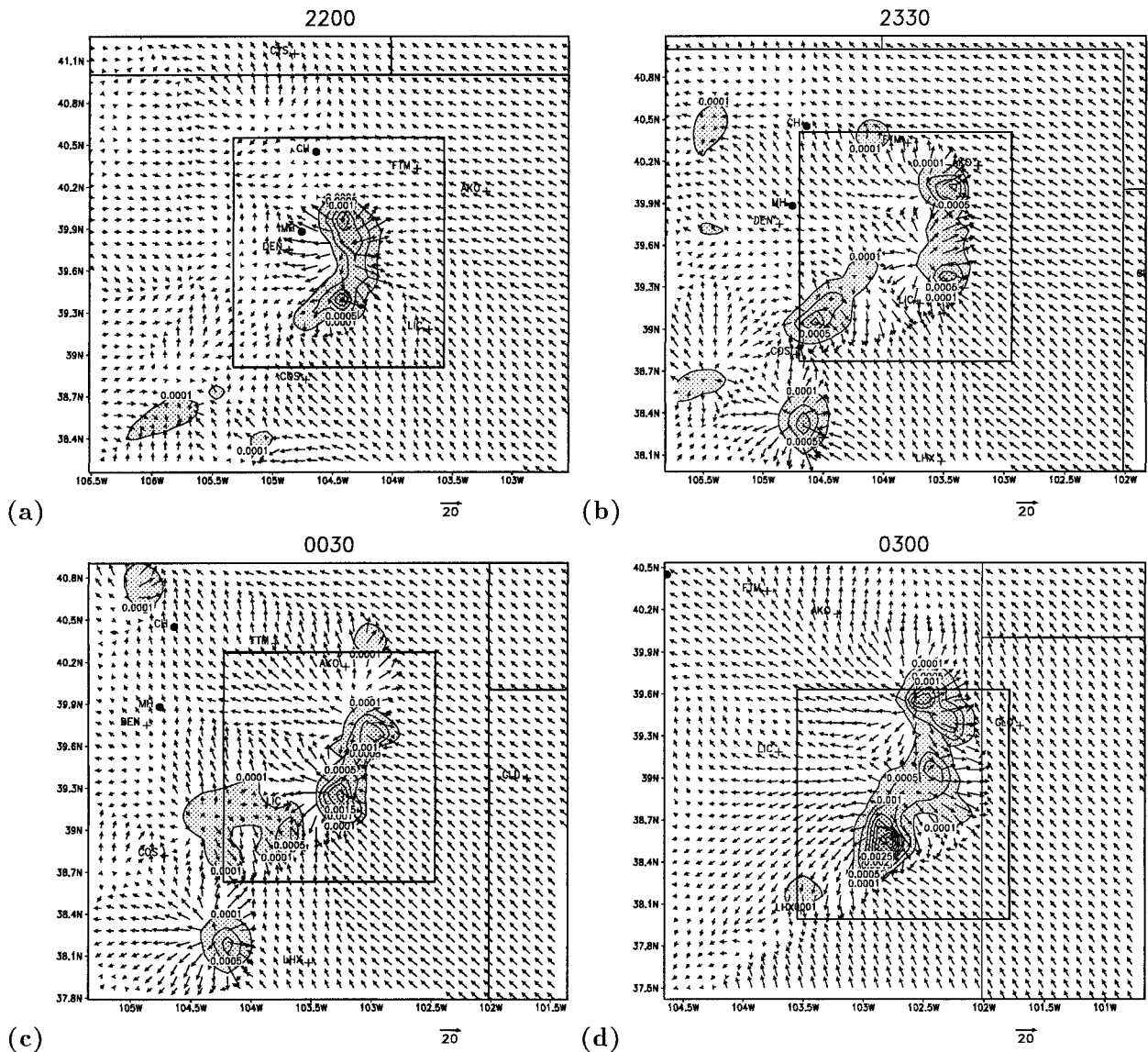


FIG. 5. Total condensate and ground relative wind vectors on grid 3 at the lowest σ level (49 m AGL). The times plotted are (a) 2200, (b) 2330, (c) 0030, and (d) 0300. The locations of the CHILL (CH) and Mile High (MH) radars as well as a few NWS reporting stations are plotted. The position of grid 4 is indicated by the rectangle. Total condensate greater than 0.1 g kg^{-1} is shaded, and values above 0.5 g kg^{-1} are contoured at 0.5 g kg^{-1} increments. Vectors are plotted in m s^{-1} according to the scale at the bottom of each panel.

2333. The simulated mass flux went through a minor cycle at about the same time, but the negative tendencies were not as large. After 0000, the simulated trend reversed and the mass flux steadily increased to a maximum at 0200. The disagreement with the observations was likely due to the observed system leaving the dual-Doppler analysis region. Reflectivity-derived rainfall rates continued to increase through this period as the new cells developed along the southwestern portion of the line. Satellite-observed cold cloud tops also expanded between 2300 and 0100 (Fig. 5 of Part I). This evidence indicates that the mass flux in the observed system was likely intensifying through the period. The

model results show that this intensification occurred as the MCS propagated into the low-level jet. At 2300, the ambient moisture and northward (v) wind component feeding into the system at 1300 m AGL were 7 g kg^{-1} and 8 m s^{-1} , respectively. By 0100, these had increased to 9.6 g kg^{-1} and 18 m s^{-1} .

4. MCS-generated propagating disturbances

In Part I, the existence of rearward propagating low-frequency gravity waves was hypothesized based on the dual-Doppler winds. Although the waves themselves were not observed, upper-tropospheric front-to-rear and

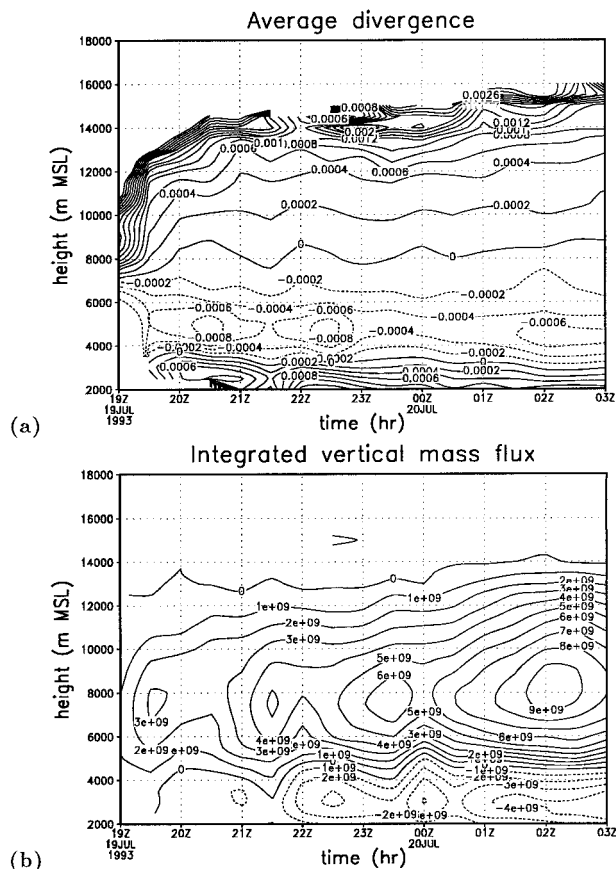


FIG. 6. (a) Time series of simulated MCS-average divergence profiles. Contours are every 0.0002 s^{-1} . (b) Time series of simulated MCS area-integrated vertical mass flux. Contours are every $1 \times 10^9 \text{ kg s}^{-1}$.

midtropospheric rear-to-front velocity perturbations suggested the presence of waves. The development of these perturbations can be investigated more thoroughly with the model data. Unlike the Doppler data, subtle vertical motions were resolved through the entire grid in both cloudy and clear regions at very high time resolution.

The similarity between the vertical structure of the simulated and observed average divergence profiles indicates the dominant gravity wave modal structure should also be similar (Mapes 1993). Nicholls et al. (1991) and Pandya and Durran (1996) found that the strength of the leading edge vertical motions in the internal gravity waves was proportional to the time derivative of the convective heating. Not surprisingly, the most significant wave events in this simulation were found during large changes in convective vertical mass flux. Convection was constantly pulsating, but the largest wave fronts were produced when most of the convective cells intensified together, producing a system-wide increase in mass flux (Fig. 6b). Three major events stood out during the simulated system lifetime. The first and weakest event occurred shortly after 1900 as con-

vection first developed in the relatively quiescent atmosphere. The second event occurred between 2100 and 2200 when the north-south convective line rapidly developed southeast of Denver, and the third event occurred after 0000 20 July as convection intensified upon intercepting the low-level jet.⁴ The first two events were quite similar in that they were dominated by linear gravity waves. Although the storm-relative upper-tropospheric flow behind the line was reduced by the passage of the waves, it was not reversed. The later of these two events is described herein⁵ since it coincided with the period of Doppler observations. The third event, described in section 3b, was unique in several ways. The resulting upper-tropospheric horizontal mass divergence was strong enough to completely reverse the storm-relative flow, producing a large, oval cold cloud shield as it did so. This event also displayed strong nonlinear characteristics, indicating a direct injection of mass and momentum into the upper troposphere.

a. The 2100–2200 event

The rapid development of the convective line between 2100 and 2200 southeast of Denver was well simulated, although the timing of the modeled storm was about 30–60 min fast. Figure 7 shows the midlevel perturbation flow in the simulated storm as it reached a geographical location similar to that shown in Fig. 17 of Part I. Perturbation winds and potential temperatures in the model were calculated by subtracting the average values at each height on grid 2 from the simulated total fields. As discussed in Part I, the effects of the gravity waves were best observed in this reference frame.

The convective lines in both systems were bow shaped and similar in meridional length (88 and 96 km for the observed and simulated lines, respectively). Perturbation flow converged toward the convective line from the east and west, although significant easterly perturbations only extended for a few kilometers ahead of the line. Behind the line, simulated westerly perturbations extended over 60 km into the condensate-free air. Moderate rear inflow was observed at the back edge of the reflectivity (Fig. 17 of Part I); however its full extent could not be measured due to the lack of radar scatterers. The lack of strong momentum gradients at the back edge of the radar reflectivity suggested that the perturbation wind pattern extended into the echo-free air, as it did in the simulated storm. Line-perpendicular vertical cross sections (Fig. 8; Figs. 14 and 19 of Part I) indicate that the strongest momentum perturbations were on the western side of both systems. The perturbation flow consisted of upper-tropospheric front-to-rear

⁴ The mass flux pulse at 2330 was mainly due to the intensification of a small portion of the convective line and gravity wave activity was limited.

⁵ The first event is discussed in Nachamkin (1998).

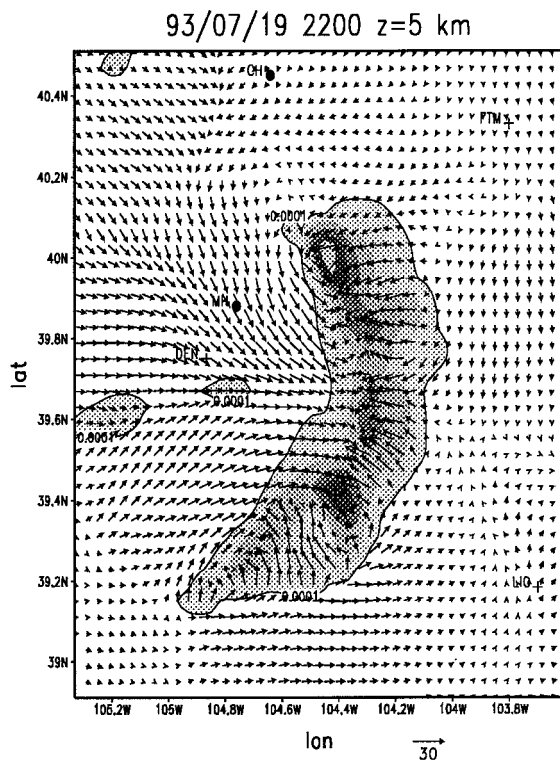


FIG. 7. Perturbation wind vectors and total model condensate on grid 4 at 2200 at a constant height of $z = 5$ km MSL. Winds were derived by subtracting the averaged winds on grid 2 at this level. Vectors are scaled at the bottom of the figure. Total condensate is shaded at 0.5 g kg^{-1} increments at and above 0.5 g kg^{-1} , the 0.1 g kg^{-1} level is also shaded. The locations of meteorological reporting stations are denoted by plus signs and the three-letter ID. The locations of the CH and MH radars are denoted by dots.

and midtropospheric rear-to-front branches superimposed upon the ambient environmental winds. This flow organization was not as apparent in either the simulated (Fig. 8a) or observed (Fig. 14a of Part I) storm-relative winds. The perturbation flow structure indicates that the majority of the low-frequency gravity wave energy was propagating to the rear of the line as described by Pandya and Durran (1996). Such propagation was independent of the anvil condensate, the majority of which was advecting ahead (east) of the line at this time.

Since the gravity waves were themselves resolved in the model data, any preferential westward propagation could be directly investigated. The vertical motions were rather subtle; however the large, deep low-frequency wave fronts were located by averaging in both the vertical and horizontal directions. Vertical motions between the 5- and 10-km levels (Fig. 9) depicted the horizontal extent of the waves, while the vertical wave structure was revealed by averaging along the line (Fig. 10). Between 2120 and 2200, three distinct pulses were emitted by convection, and at 2200 were located at approximately 105.3° , 105° , and 104.7°W (A–C in Figs. 9 and 10). The average phase speed of $\sim 17 \text{ m s}^{-1}$ was

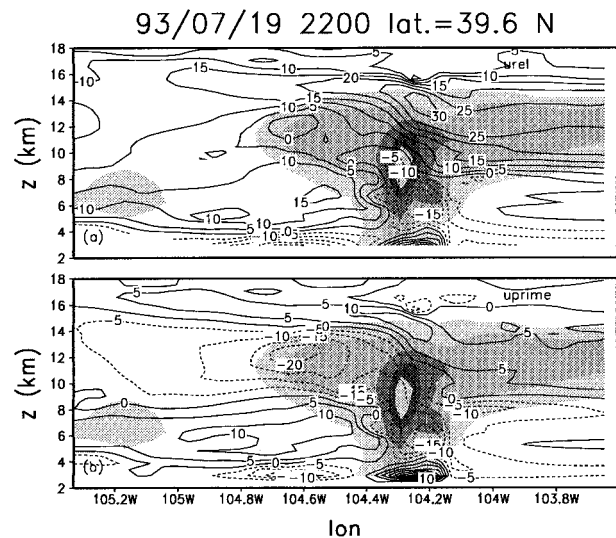


FIG. 8. Vertical x - z cross sections on grid 4 at 2200 at $y = 39.63^\circ$ lat. (a) Storm-relative winds are contoured at 5 m s^{-1} increments. (b) Winds relative to the grid 2 average at each respective level are contoured at 5 m s^{-1} intervals. Total condensate is shaded in each panel at 0.5 g kg^{-1} increments at and above 0.5 g kg^{-1} , and the 0.1 g kg^{-1} level is also shaded.

considerably slower than the 30 m s^{-1} deep mode phase speeds discussed by Mapes (1993). Similar phase speed calculations were conducted for this environment using $N^2 = (g/\Theta)(\partial\Theta_v/\partial z)$. Cloud effects were not included since the waves were generally traveling through unsaturated air. The meridionally averaged N west of the convective line was about 0.009 s^{-1} between the boundary layer top and the tropopause. The value of H was chosen to be 10 km, as it was the average depth of the simulated convection at 2200 UTC. These values resulted in phase speeds of 28.6 and 14.3 m s^{-1} for the n_1 and n_2 modes, respectively, which is quite close to Mapes (1993). Since the actual waves were propagating upwind in a sheared inhomogeneous environment, the phase speeds were likely reduced (e.g., Schmidt and Cotton 1990).

All three pulses originated from cells within the newly formed portion of the convective line north of 39.5° lat. Each pulse appeared during times of intense cell growth or decay, with downward (upward) branches emanating from strengthening (weakening) storms. The strong upward branch (B in Figs. 9 and 10) that appeared shortly before 2136 was initiated by a decaying cell at the northern end of the line. As this and the other waves expanded westward, vertical motions along their leading edges rapidly broadened and weakened. Subtle potential temperature perturbations propagated outward with the waves, with warming and cooling associated with downward and upward⁶ motions, respectively. A pulse of

⁶ Although midtropospheric temperatures fell with the passage of the upward motions, the net perturbation was still positive.

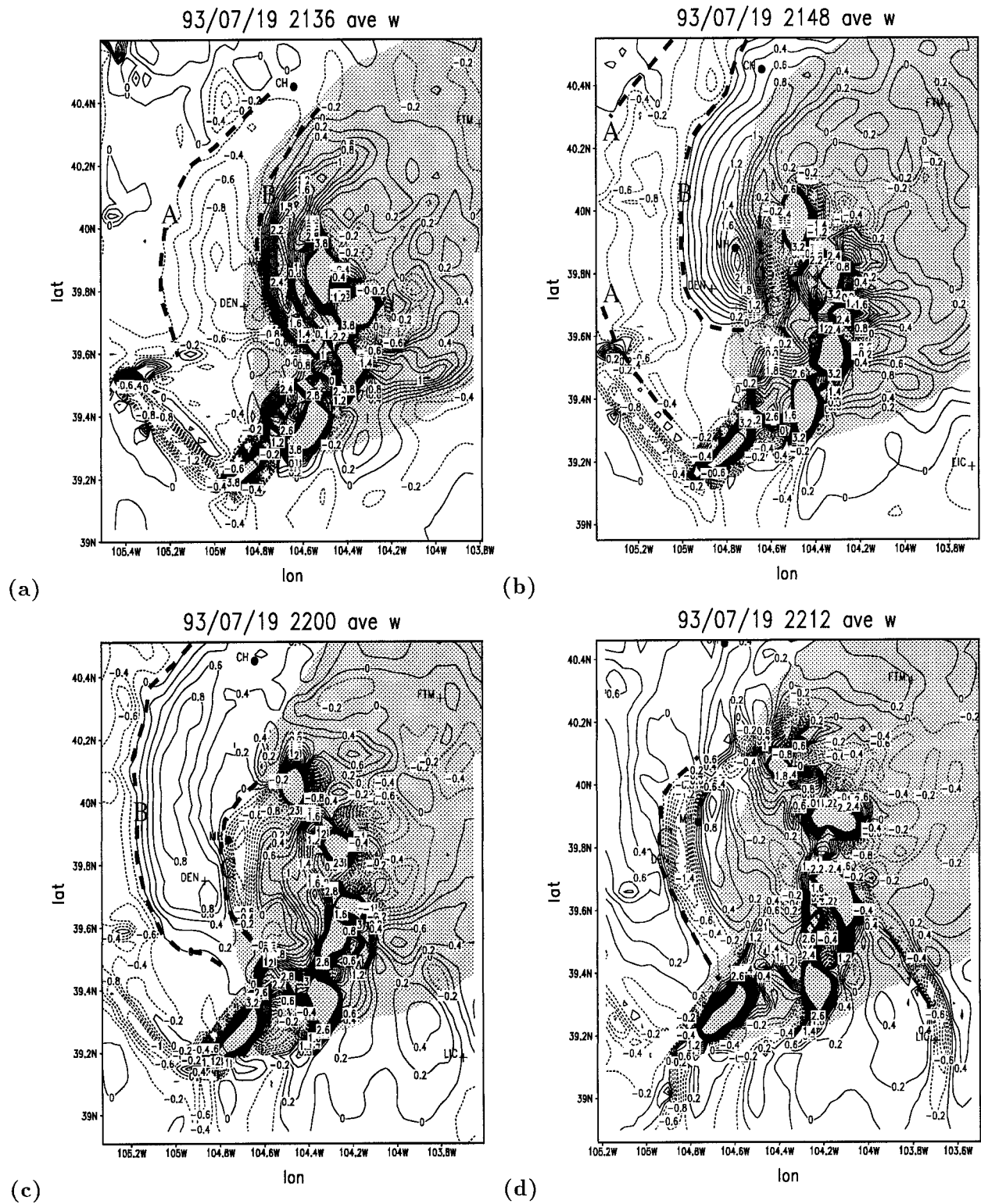


FIG. 9. Vertically averaged vertical motion between $z = 5$ and $z = 10$ km MSL on grid 4 at (a) 2136, (b) 2148, (c) 2200, and (d) 2212 UTC. Vertical motions between ± 4 m s^{-1} are contoured at 0.2 m s^{-1} intervals. Total condensate greater than 0.1 g kg^{-1} at 10 km is shaded. Heavy dashed, labeled lines indicate the approximate leading edges of gravity wave disturbances in the vertical motion field.

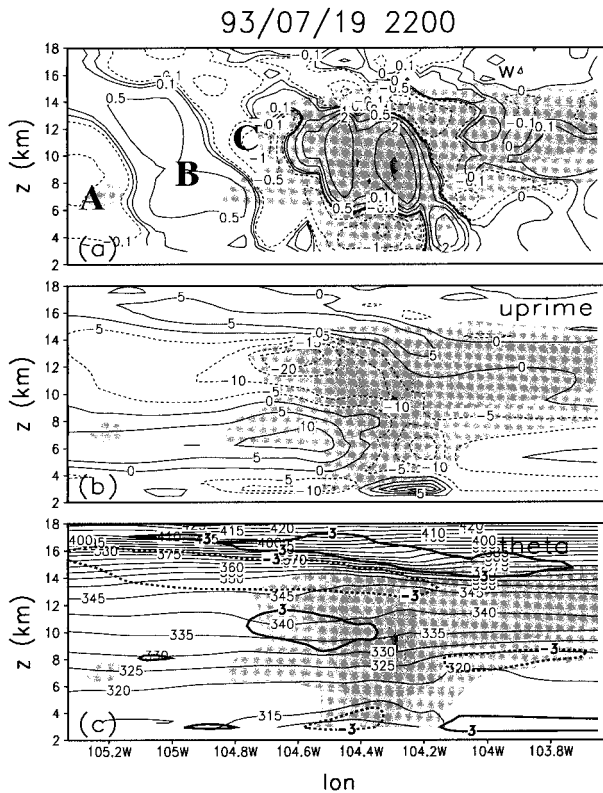


FIG. 10. Vertical x - z cross sections on grid 4 at 2200 derived by meridionally averaging (a) vertical motion, (b) perturbation flow (relative to the grid 2 environmental mean at each level), and (c) potential temperature. The averaging interval was from 39.5° to 40.1° lat. Averaged total condensate is shaded at 0.5 g kg^{-1} increments at and above 0.5 g kg^{-1} . The 0.1 g kg^{-1} level is also shaded. All positive (negative) contours are solid (dashed). Perturbation potential temperatures of $\pm 3 \text{ K}$ are depicted by heavy contours in (c). The labels A-C correspond to the labeled disturbances in Fig. 9.

warming between 8 and 13 km can be seen trailing downward branch C, which was just exiting the western edge of the anvil at 2200 (Fig. 10c). Like the vertical motion field, the temperature anomalies rapidly broadened and weakened as the wave fronts propagated away. Average mid- and upper-tropospheric potential temperatures within the condensate were not much higher than the ambient environment, indicating that most of the latent heating was propagating away with the gravity waves.

Perturbation horizontal flow at all levels behind the line (Figs. 10 and 11) was affected by the passage of each wave front; downward branches increased the upper-tropospheric front-to-rear and midtropospheric rear-to-front perturbations, while the upward branch induced opposite tendencies. This resulted in rearward propagating anomalies in the front-to-rear and rear-to-front flows, not unlike that observed by Klimowski (1994). The effects were most pronounced above 10 km. Even at that level, velocities were affected by competing factors, especially close to the convection. However, as the

pulses propagated away from the system, the responses in the perturbation velocity field were more clearly associated with the pulses. The vertical motions within the pulses appeared to be dominated by the $n1$ mode, but time-varying heights of the maxima and minima within each pulse indicate that several modes of different speeds were superimposed. Horizontal winds, which respond to the integrated net wave forcing, also indicated the presence of higher-order ($\sim n2$) energy. The elevated rear inflow perturbations (Fig. 10b), for example, are intrinsically $n2$ in structure (Mapes 1993).

Relatively little low-frequency wave activity existed to the east of the line.⁷ Only one eastward propagating wave of this type was detected, and it occurred with the first convective development. It took on the shape of a complete roll, indicating that the heating structure that produced it was finite in time (Nicholls et al. 1991). No other detectable low-frequency waves propagated east of the line through the rest of the simulation. Thus, the wave-induced net effects on the perturbation fields were close to zero.

Schmidt and Cotton (1990) noted that the strongest gravity waves occur on the trailing side of the convective line. Idealized experiments indicate that these asymmetries result from the structure and orientation of the heat source. Pandya and Durran (1996) found that a deep rearward-leaning heat source trailed by a shallower rearward-leaning heat sink (a structure commonly found in many squall lines) produced the strongest low-frequency energy in the direction of tilt. In a similar experiment Fovell et al. (1992) found that waves generated by an oscillating cylindrical source experienced the same effect when the oscillator was propagating or tilted out of the vertical. In the case studied here, new updrafts frequently built on the eastern side of existing convection, and precipitation fell to the west (Fig. 10a; Figs. 14, 19, and 23 of Part I). This suggests a heating profile similar to Pandya and Durran (1996).

Strong vertical shear could also have distorted or hidden the effects of the downshear waves. However, since the observable effects from one such wave were simulated, it is not likely that the effects from all subsequent waves would be hidden. As an additional test, a simple nonlinear, two-dimensional, horizontally homogeneous simulation was conducted with an idealized heat source. The heating was defined by

$$Q_z = Q_0 \left[\sin\left(\frac{\pi z}{H}\right) - \sin\left(\frac{2\pi z}{H}\right) \right], \quad (2)$$

where Q_0 and H were set to 100 K h^{-1} and 10 km, respectively. The basic formulation was similar to Nicholls et al. (1991) in that both the $n1$ and $n2$ modes were

⁷ The arcing region of downward motion just southeast of the line at 2212 (Fig. 9d) was anchored above a developing boundary layer convergence zone, and was not a propagating gravity wave.

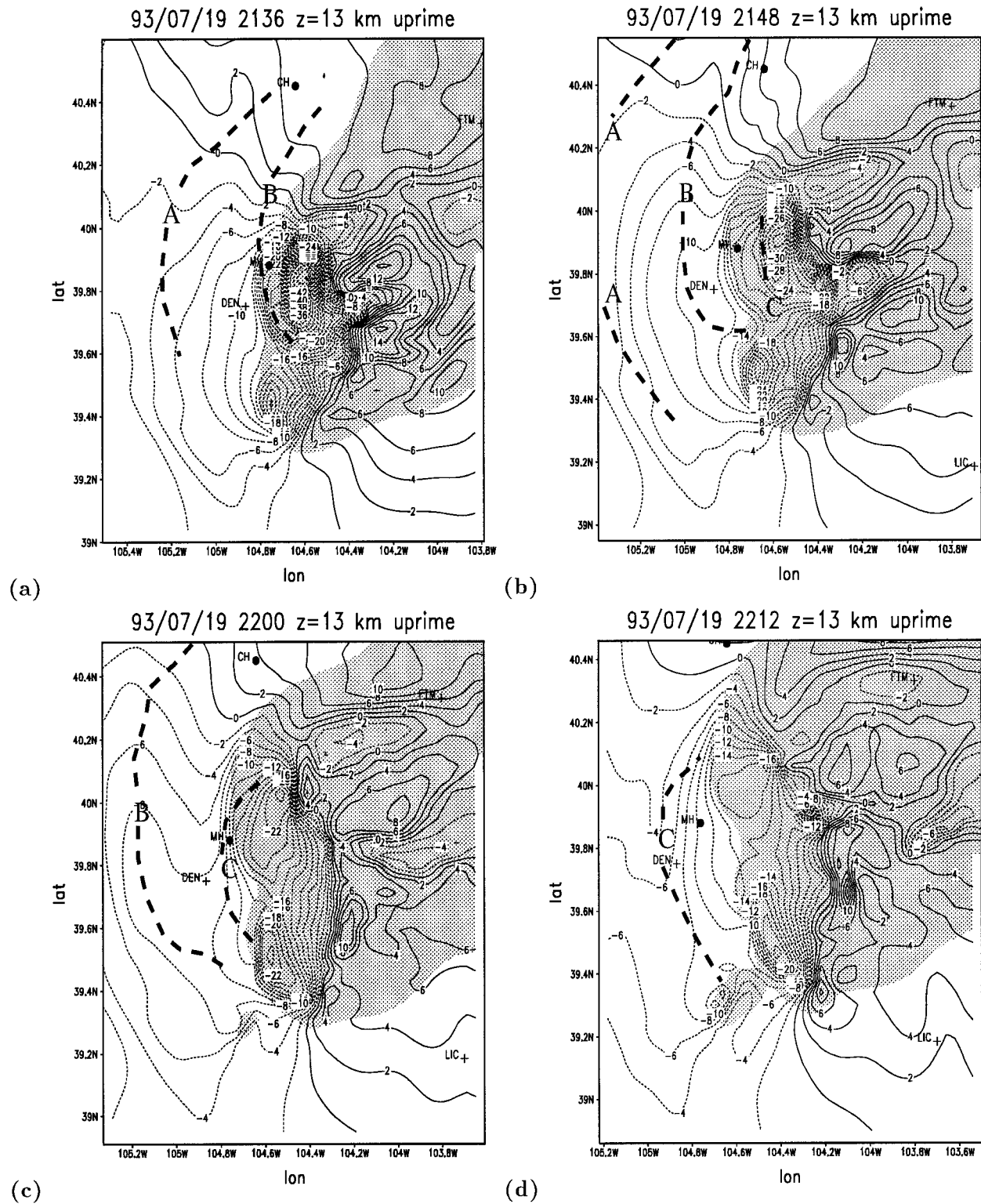


FIG. 11. Perturbation u -component wind speed at 13 km MSL on grid 4 at (a) 2136, (b) 2148, (c) 2200, and (d) 2212 UTC is contoured at 2 m s^{-1} intervals. Total condensate greater than 0.1 g kg^{-1} at 13 km is shaded. As in Fig. 9, heavy dashed, labeled lines indicate the approximate leading edges of gravity wave disturbances in the vertical motion field.

included. The environment was initialized with a sounding taken from the MCS simulation about 100 km south-east of the system. The homogeneous simulation was run for 2 h, with the heating slowly increasing to its maximum values over the first half hour. Although the wave fronts were considerably distorted by the shear, the perturbation u -velocity field after 2 h reflected strong gravity wave propagation in both directions. Thus, as Pandya and Durran (1996) suggest, shear alone is not enough to produce the asymmetries in two dimensions.

b. The 0100–0200 event

Between 0000 and 0200 the MCS crossed into the axis of the low-level jet. As a result, convection rapidly intensified after 0000, with the strongest growth occurring in the back-building storms in the southwestern portion of the system. The ensuing response away from convection was dominated by an intense upper-tropospheric disturbance that expanded outward from the convective line (Figs. 12, 13, and 14). The majority of the temperature and momentum perturbations with this disturbance pushed westward directly into the strong flow. By 0200 the western edge of the anvil shield was defined by the sharp arc-shaped feature located near -103.6° longitude.⁸ Although this evolution occurred beyond the range of the dual-Doppler coverage, the simulated anvil expansion was very similar to the rapid expansion of the coldest satellite cloud tops observed between 2300 and 0200 (Fig. 5 of Part I).

The disturbance associated with the anvil expansion was different from the deep gravity waves that had dominated up to this point. It was strong enough to reverse the upper-tropospheric storm-relative flow, allowing for the development of significant trailing anvil in its wake. Temperature and momentum perturbations did not rapidly diffuse to the far field as they did in the gravity waves at 2200. Instead, upper-tropospheric perturbation horizontal flow (Fig. 14) expanded westward like an advective outflow, with the western edge remaining sharply defined for over 1.5 h. Upper-tropospheric potential temperatures warmed by over 6 K and lower-stratospheric potential temperatures cooled by 5–10 K in the wake of the disturbance. Lapse rates within the anvil approached dry adiabatic⁹ reflecting the spread of a large, warm plume aloft. None of the rearward propagating gravity waves to this point generated such a focused response so far outside the convection.

Vertically averaged vertical motions indicated little deep ($\sim n1, n2$) low-frequency wave activity. The strongest signals came from the 10–13-km layer in the form

of a propagating pulse of downward motion (Fig. 12). Like the horizontal momentum and temperature anomalies, vertical motions within the pulse remained nearly constant in strength until it approached the grid boundary. The vertical structure of the disturbance (near -103.6° long in Fig. 13) was difficult to classify due to interfering motions from weaker convection trailing the system. The couplet of downward and upward motion above and below 8 km was similar to an $n2$ mode. However, the strong front-to-rear flow immediately trailing the upper-tropospheric downward motion did not have a corresponding midtropospheric rear inflow maximum. Instead, fairly uniform rear inflow behind the dissipating western convection merged with the main line and intensified in situ beneath the leaning updraft, similar to that observed by LeMone (1983).

While the nondiffusive nature of the upper-tropospheric disturbance is not necessarily evidence against it being a gravity wave, many characteristics of this disturbance indicate that it was advective, or nonlinear, in nature. This is not surprising given that the strong momentum gradient retained its continuity within grid 4 for over 1.5 h. Compare that with the modes at 2200, which weakened and moved out of the grid within 30 min. As a simple, quantitative test for nonlinearity, a few linear and nonlinear terms from the equations of motion as well as the thermodynamic equation were calculated in the upper troposphere near the western edge of the disturbance. Model data from 0200 were used, the mean state was estimated from the average over grid 2, and all derivatives were taken on constant height surfaces. Values for the linear terms were estimated as $\partial u/\partial t \sim 0$,¹⁰ $\bar{u}\partial u'/\partial x \sim -0.07 \text{ m s}^{-2}$, $\rho_0^{-1}\partial p'/\partial x \sim 0.02 \text{ m s}^{-2}$, $\partial\theta/\partial t \sim 0.001 \text{ K s}^{-1}$, $\bar{u}\partial\theta'/\partial x \sim 0.046 \text{ K s}^{-1}$, and $w'd\bar{\theta}/dz \sim -0.014 \text{ K s}^{-1}$. The nonlinear terms involving the horizontal advection of momentum and temperature were estimated to be of the same order of magnitude as the linear terms, for example, $u'\partial u'/\partial x \sim -0.07 \text{ m s}^{-2}$, and $u'\partial\theta'/\partial x \sim -0.037 \text{ K s}^{-1}$. Thus, it is not likely that this late disturbance was a linear gravity wave like those described by Nicholls et al. (1991) and Mapes (1993). In contrast, similar calculations from several of the more wavelike disturbances at 2200 yielded nonlinear terms that were an order of magnitude smaller than their linear counterparts.

5. MCS effects at large distances

To investigate the cumulative effects of convection away from the MCS, the environmental gradients on grid 2 were removed by subtracting the results of a non-microphysics simulation. This run was identical to the full MCS run except that all condensation, and thus

⁸ Anvil cloudiness in the southwestern portion of the grid prior to 0130 was associated with weak convection to the southwest of the main system (Figs. 5b,c).

⁹ Moist- and dry-adiabatic lapse rates were approximately equal above 10 km.

¹⁰ The western edge of the disturbance was nearly stationary with respect to the ground at this time.

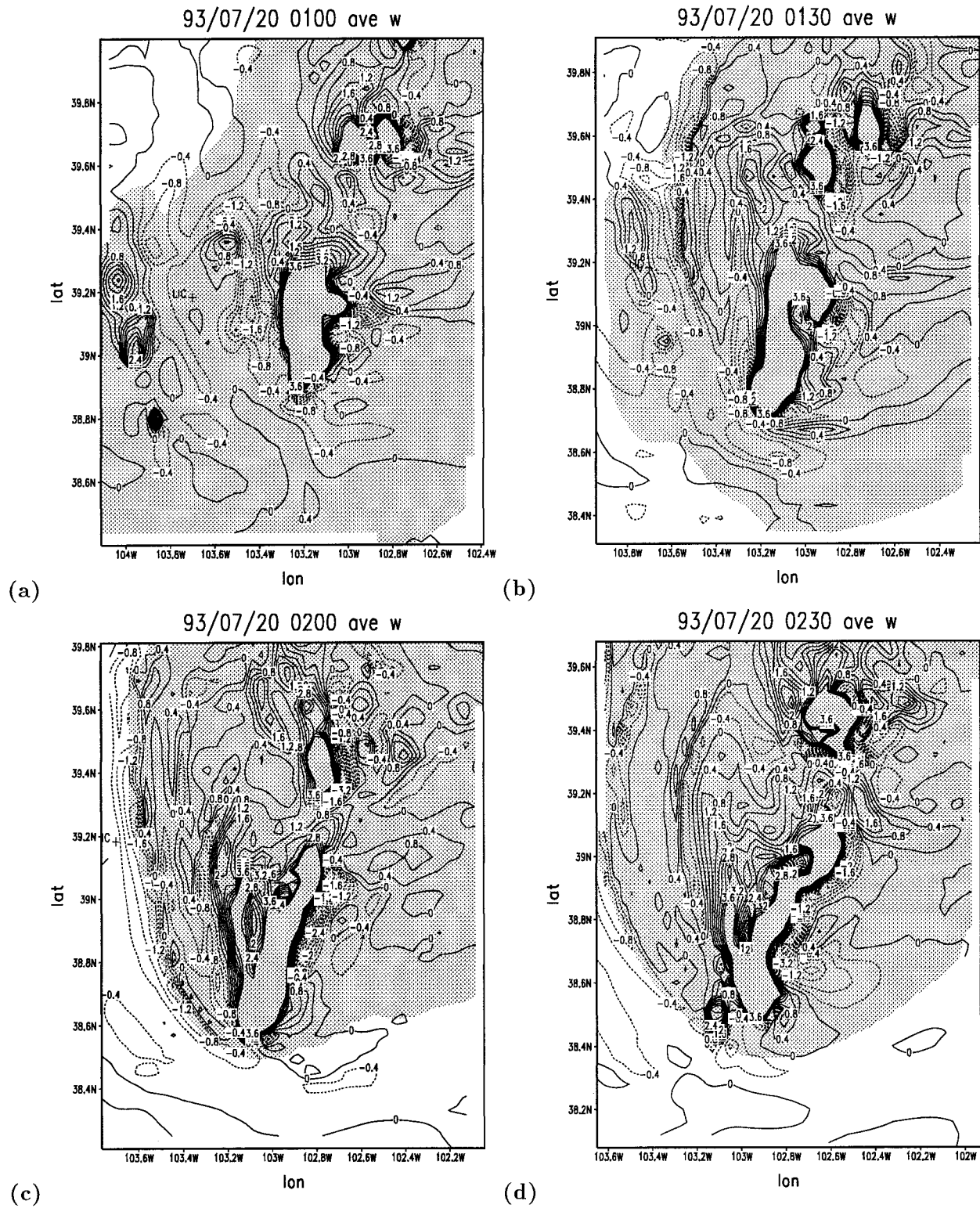


FIG. 12. Vertically averaged vertical motion between $z = 10$ and $z = 13$ km MSL on grid 4 at (a) 0100, (b) 0130, (c) 0200, and (d) 0230 UTC. Vertical motions between ± 4 m s⁻¹ are contoured at 0.4 m s⁻¹ intervals. Total condensate greater than 0.1 g kg⁻¹ at 13 km is shaded.

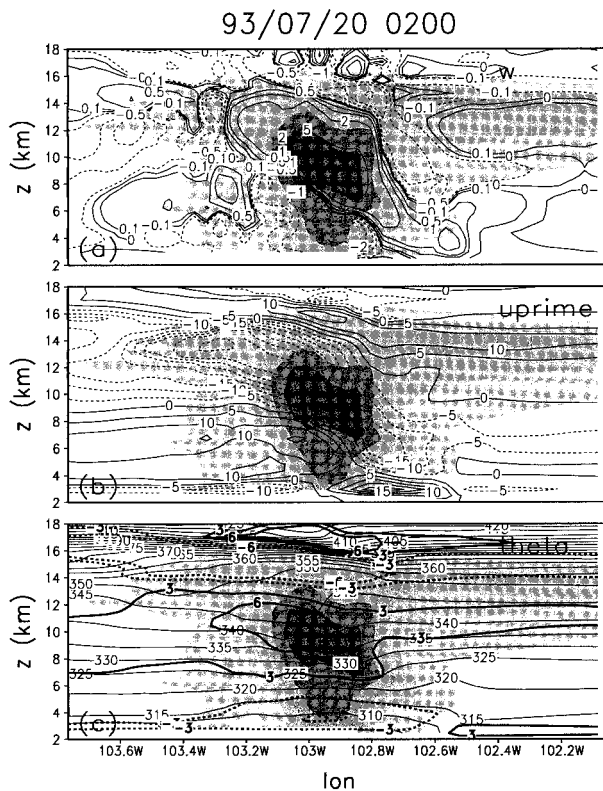


FIG. 13. Vertical x - z cross sections on grid 4 at 0200 derived by meridionally averaging (a) vertical motion, (b) perturbation flow (relative to the grid 2 environmental mean), and (c) potential temperature. The averaging interval was from 38.8° to 39.2° lat. Averaged total condensate is shaded at 0.5 g kg^{-1} increments at and above 0.5 g kg^{-1} . The 0.1 g kg^{-1} level is also shaded. All positive (negative) contours are solid (dashed). Perturbation potential temperatures of ± 3 and $\pm 6 \text{ K}$ are depicted by heavy contours in (c).

convection, was excluded. This was in essence a separate way of looking at the environmental perturbations created by convection. The main advantage over simply subtracting out the grid 2 average fields is that the horizontal storm-induced perturbations are not overwhelmed by the environmental gradients. The main disadvantage is that the ambient environment may evolve differently without the MCS. In this case, the environmental evolution in both the wet and dry simulations was similar. The main differences were located in the boundary layer close to the mountains, where the mountain-plains solenoid was stronger and shallower in the dry run. In their sensitivity studies, Tripoli and Cotton (1989) similarly found that the mountain-plains solenoid remained shallow and locked to the topography in the absence of convection. The main effect in the case studied here was an increase in the dry run boundary layer upslope in mountainous regions. This effect appeared to exert only minor influences in the mid- and upper troposphere, where the bulk of the analysis was concentrated.

At large distances from the MCS, the majority of the

perturbations were associated with the propagating gravity waves. Given the wave propagation asymmetries, it is not surprising that almost all of the mid-tropospheric warming occurred to the west of the convective line (Figs. 15 and 16). Positive potential temperature perturbations up to 1 K extended out to 300 km , with maximum perturbations reaching 5 K . Perturbation flow behind the system was relatively weak at 8 km , as this level was close to the inflection between front-to-rear and rear-to-front perturbation flows (Fig. 16). Averaged east-west vertical cross sections (Fig. 16) show the gravity wave quadrature, with maximum perturbation velocities located at the temperature inflections. This pattern extended well into the stratosphere, indicating vertical wave propagation. As in the troposphere, the stratospheric wave signatures were confined to the western side of the system.

Mean meridional asymmetries across the MCS (Fig. 17) differed from the zonal asymmetries in several ways. Mid-tropospheric warm anomalies were mostly confined to the region within the condensate, with only 1 - 2 K anomalies extending northward from the system. Lower-stratospheric cool perturbations of up to 2 K extended somewhat farther north, but there was little evidence of vertical propagation in this area. Strong southerly momentum perturbations extended along the upper troposphere north of the anvil, reaching maximum speeds of 12 m s^{-1} just outside the condensate. Unlike the zonal cross sections, the speed maximum was located outside the contiguous anvil. This is not atypical for an MCS, as jet streaks often develop to the north of these systems (Maddox 1983). On the southern side of the system, momentum and temperature perturbations were much weaker and remained close to the condensate. Some vertical propagation was evident as thermal and momentum perturbations tilted upward into the lower stratosphere.

The lack of vertical propagation to the north, as well as the consistent occurrence of wind maxima outside the system, suggests that gravity waves were not directly responsible for the meridional asymmetry. Blanchard et al. (1998) suggest that weak upper-tropospheric inertial stability results in the development meridional circulations on the northern side of an MCS. It is possible that this mechanism was operating here since the absolute vorticity of the ambient flow was near zero in this case. A large region of negative absolute vorticities was also simulated to the north of the anvil.

Simulated environmental effects like those discussed above are difficult to verify with the coarse standard observational network. However, the 0000 UTC 20 July Denver sounding (Fig. 18a) was ideally located to sample the temperature structure west of the system. A simulated sounding taken near Denver at 0200¹¹ (Fig. 18b)

¹¹ This sounding was taken later to be in the same storm-relative position as the observed sounding.

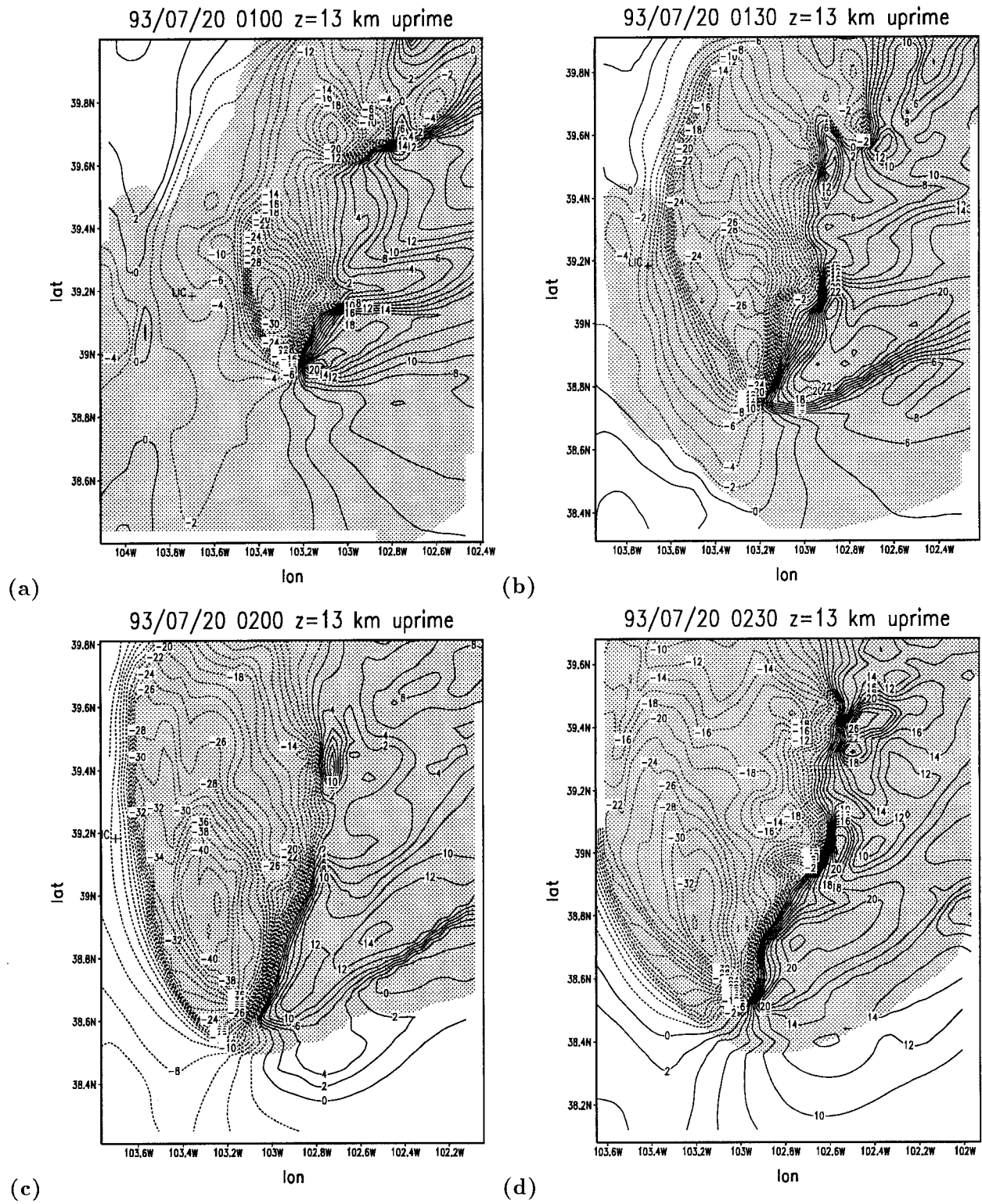


FIG. 14. Perturbation u -component wind speed on grid 4 at (a) 0100, (b) 0130, (c) 0200, and (d) 0230 UTC is contoured at 2 m s^{-1} intervals. Total condensate greater than 0.1 g kg^{-1} at 13 km is shaded.

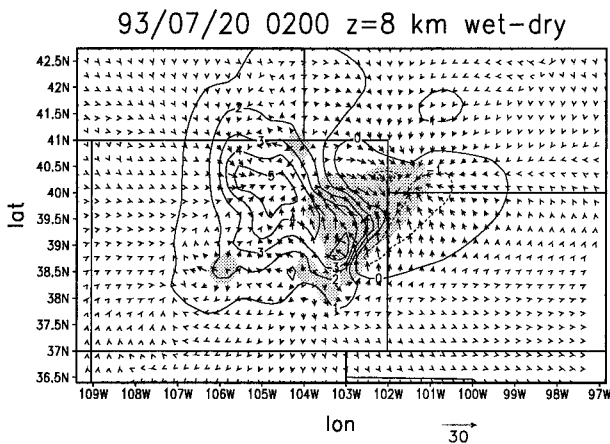


FIG. 15. Potential temperature differences between the control run and the no microphysics run (wet - dry) are contoured at 1.0-K intervals. The data are on grid 2 at 0200 at $z = 8$ km MSL. Total condensate greater than 0.1 g kg^{-1} is shaded. Wind differences between the two runs (wet - dry) are represented as vectors that are scaled in m s^{-1} at the lower right.

showed considerable agreement with the observations. Notably, both soundings contained a warmed layer above 450 hPa, with a sharp inversion at the base of observed warming (near 440 hPa in Fig. 18a). The base of the simulated warm layer was not as sharp, but the vertical grid spacing likely resulted in some smoothing. Observed temperatures in the warmed layer were 3° – 5°C higher than their morning values, which is consistent with the magnitude of the simulated warming. Moreover, this warm layer was completely absent from the North Platte sounding (LBF in Fig. 2 of Part I), and only weakly apparent at Dodge City (DDC in Fig. 2 of Part I). Several small convective cells south of DDC at 0000 were likely affecting the local environment and may have been responsible for the weak warming there. On a related note, the authors have observed that some MCSs leave distinct dry wakes for hundreds of kilometers in the satellite-observed upper-tropospheric water vapor. The drying associated with the focused subsidence warming in the 0000 DEN sounding may be indicative of the formation of such a wake.

6. Discussion and conclusions

By many measures, this MCS and its surrounding environment were well simulated. The synoptic-scale height and wind patterns agreed well with the observations, as did the evolution of the MCS precipitation and momentum fields. It is, in fact, quite a feat that features at scales of 10–20 km were simulated well at all. As discussed in Part I and by Nachamkin and Cotton (1998), strong, topographically forced circulations such as the mountain-plains solenoid, the Palmer Divide-Platte Valley solenoid, and the Denver Cyclone (Szoke et al. 1984) were important to the formation of this system. Simulation of these features is dependent on

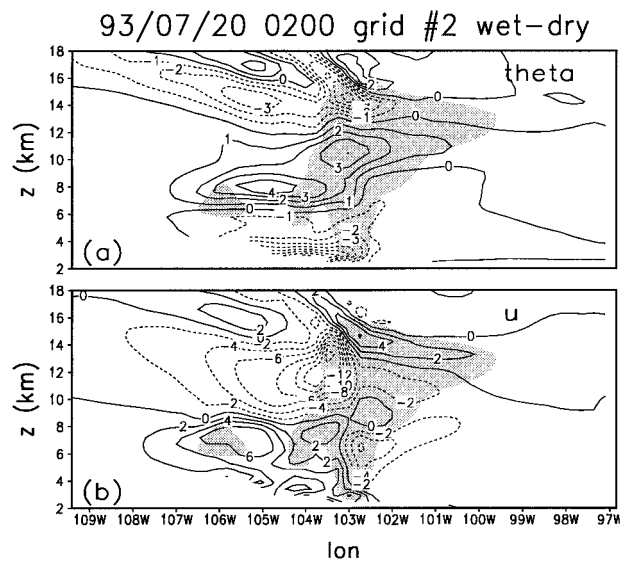


FIG. 16. East-west (x - z) vertical cross sections on grid 2 at 0200. Difference fields of (a) potential temperature and (b) u wind components between the control and the no microphysics (wet - dry) runs are plotted. The fields have been meridionally averaged between 38° and 41° lat. Averaged total condensate greater than 0.1 g kg^{-1} is shaded.

physiographic forcing at the lower boundary, and error growth from the initial conditions can be alleviated. This does not mean that every convective updraft or gravity wave was exactly reproduced by the model. However, the integrated environmental effects were very similar

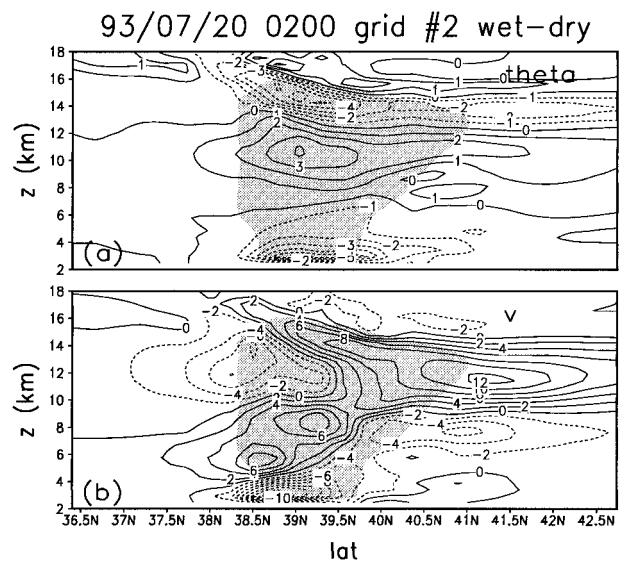


FIG. 17. North-south (y - z) vertical cross sections on grid 2 at 0200. Difference fields of (a) potential temperature and (b) v wind components between the control and the no microphysics (wet - dry) runs are plotted. The fields have been zonally averaged between 101.5° and 104°W . Averaged total condensate greater than 0.1 g kg^{-1} is shaded.

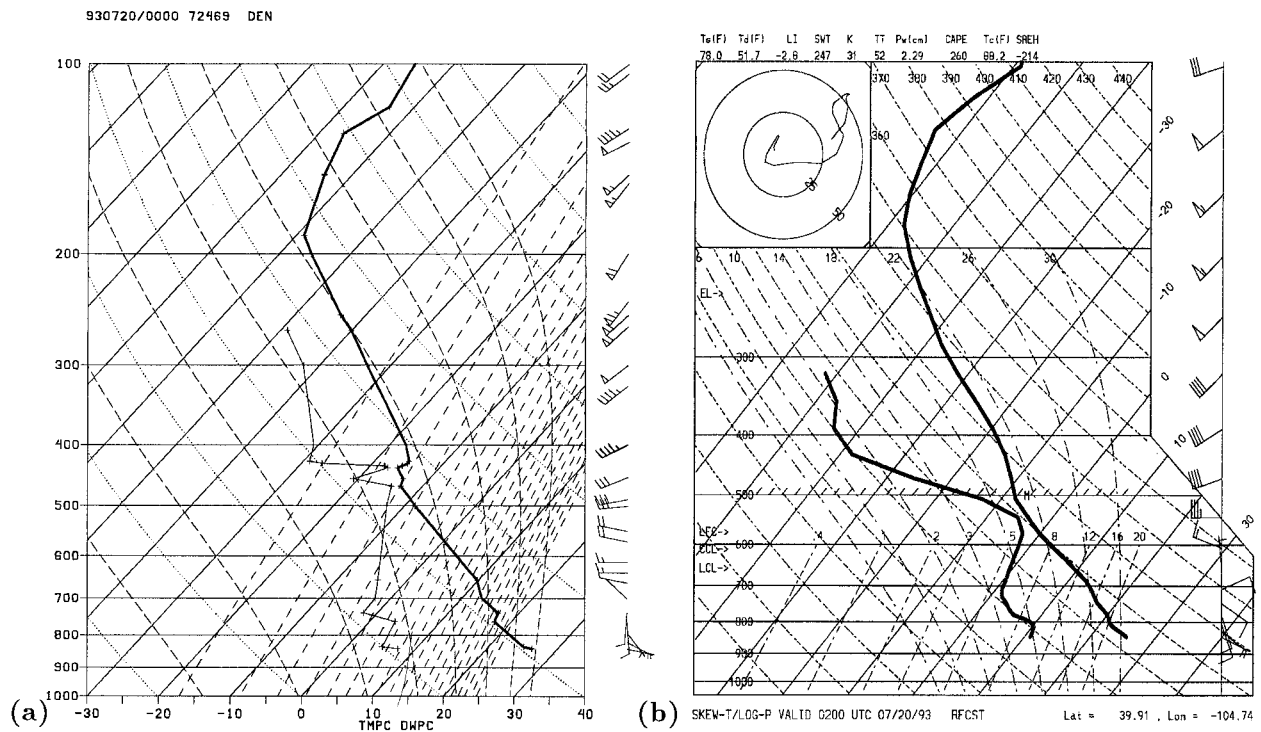


FIG. 18. Thermodynamic soundings from (a) the Denver 0000 20 Jul observation, and (b) the closest grid point to Denver on grid 2 at 0200.

in both cases. In this light, the observed and simulated MCSs are best thought of as separate, but similar, events.

Data from the model and the observations show that compensating momentum and temperature perturbations away from the MCS condensate region were largely the result of rearward-propagating gravity waves. Upper-tropospheric perturbation outflow and midtropospheric perturbation inflow developed predominantly on the trailing side of the system, as did a region of upper-tropospheric warming. In the model data, these features were induced by successive westward-propagating pulses of deep vertical motion, much like those investigated by Nicholls et al. (1991). The dominant westward propagation of the low-frequency waves appears to be related to the aggregate structure of the latent heating. Pandya and Durran (1996) suggest that a specific type of rearward-leaning heating profile directs gravity wave energy toward the trailing wake of the system. However, it should be noted that the pulsating nature of the wave propagation is not considered by the idealized experiments of Pandya and Durran (1996). In those experiments, the leaning aggregate heat source was simulated through the use of a time-averaged heating profile. Thus although the net effects of the aggregate are simulated, the actual process by which the individual wave fronts interact is not. This is important because although the aggregate heat source did lean westward in this case, the individual cells that produced the waves were relatively upright. Some kind of wave cancellation is likely

occurring, although no rigorous experiments were performed in this work to examine this.

This placement of the subsidence in the wake of the system has some interesting implications. CAPE in this area is already reduced by the development of boundary layer outflow. Thus the stabilizing influences of convection are concentrated over a minimal area. In this case, convection exhibiting the rearward-leaning heating profile was very efficient at removing instability over local areas. This concentration of the stabilizing influences also shows that an ongoing MCS does not always suppress convection in an adjacent system. If a new system develops away from the gravity wave wake, it experiences only minimal reductions in CAPE. In fact, a second MCS developed on the northern flank of the one studied here. Both systems maintained their strength for several hours as they propagated eastward along parallel tracks (Fig. 5 of Part I).

The intensity of the temperature and momentum perturbations in and near the MCS anvil is in part a function of how the perturbations got there. During the early stages of this system, this communication was dominated by the gravity waves. Perturbations were induced by the passage of the wave fronts, and convectively generated heating rapidly escaped horizontally and vertically outward. After about 0000 UTC 20 July, however, the MCS interacted with the low-level jet and a different kind of disturbance propagated outward. It was much stronger and slower than the gravity waves, and

it possessed several attributes of an advective outflow. Since it did not rapidly disperse, significant heat and momentum perturbations remained close to the convective cells for a long time.

Why did such an intense upper-tropospheric outflow develop in this case? Figures 10 and 13 reveal a subtle difference in the updraft structure before and after the MCS intercepted the low-level jet. Early on, the convective line was made up of separate, erect updrafts that maintained their integrity as they propagated rearward relative to the leading outflow. This effect was smoothed somewhat by the horizontal averaging in Fig. 10; however, it was well resolved in individual cross sections. Although the averaged aggregate heat source leaned westward, each individual storm cell remained tall, narrow, and relatively erect. As each cell became detached from the main moist inflow near the gust front, the updraft lost intensity and became dominated by precipitation laden downdrafts in the lower troposphere. As the updrafts collapsed, pulses of upward motion propagated rearward at gravity wave speeds. Similar rearward-propagating downward pulses were excited as new convection developed along the gust front. This succession of multiple wave fronts can be seen in Figs. 9 and 10. Since new convection continued to develop, the mean warming from the downward pulses was greater than any cooling caused by upward pulses. This resulted in the region of net midtropospheric warming that extended hundreds of kilometers to the northwest of the system.

Once the system intercepted the low-level jet, the thunderstorm updrafts became more continuous and concentrated, and the entire updraft leaned westward as a whole. Individual turrets consolidated into a more organized mesoscale updraft (Fig. 13). Individual gravity wave events also became hard to recognize. LeMone (1983) and Rotunno et al. (1988) have shown that updrafts in mature systems tend to lean rearward en masse like this. Rotunno et al. (1988) also noted that the updrafts became less oscillatory and more continuous as the cold pool circulation began to dominate. If an individual updraft leans sufficiently, large slabs of buoyant air may detrain before reaching the level of neutral buoyancy. As discussed by Yuter and Houze (1995b), if the aspect ratio of such a parcel is sufficiently large (wide and shallow), vertical perturbation pressure gradients can cancel the buoyant force. In this situation, the parcel can remain as a warm anomaly at a relatively fixed height. The remaining buoyancy is not transferred to updraft kinetic energy, and gravity waves are not excited. As Kain and Fritsch (1998) suggest, the expanding anvil at this point could easily be considered to be an integral part of the convection in this case. It is essentially a convective plume that did not reach the level of neutral buoyancy.

One should note that the detraining slab in this case is larger than that implied by the particle fountain model put forth by Yuter and Houze (1995a–c). The Yuter and

Houze model characterizes the stratiform region as an ensemble of cumulus-scale updrafts detraining hydrometers at multiple levels. This appears to be what was happening during the early stages of the system studied here as evidenced by Figs. 9–11. Individual convective storms generated gravity waves that propagated westward, while the detrained hydrometeors advected eastward in the mean flow. The slab of detrained air at later stages (Figs. 12–14) was on the scale of the entire system, and the kinematic structure of the upper-tropospheric anvil was more uniform. The outflow was strong enough to push westward against the fast upper-tropospheric mean flow. Not only were hydrometeors advected westward, but significant momentum and temperature anomalies spread westward as well. This was different from the early stages, when the bulk of the upper-tropospheric temperature perturbations were spreading by gravity waves and not advection.

If these large detrained warm anomalies remain concentrated for a sufficient period, the atmosphere will eventually respond in a balanced fashion. It was mentioned in the introduction that the size of an MCS needed to be equal to or greater than the Rossby radius of deformation in order for the balanced circulations to develop. However, Rossby radii are generally defined by the propagation speed of the deep gravity waves. Olsson and Cotton (1997) showed that Rossby radii for these waves can be hundreds of kilometers long due to their rapid phase speeds. Thus, any balanced effects are spread diffusely over a large area. However, a Rossby radius defined by the speed of an advective disturbance, like the one observed here, would be considerably smaller than that defined from the gravity waves. Systems that are dominated by an advective expansion would not necessarily have to reach the MCC size criteria to produce a significant mesoscale disturbance.

The partitioning of the outward communication of latent heating between advective outflow and gravity waves remains unknown. Results from this case indicate that highly tilted convective updrafts may produce gravity waves at a reduced rate due to the perturbation pressure effects. Such systems may be more efficient producers of large-scale disturbances since less of the latent heating radiates away as gravity waves. For the case of a large MCC this distinction may not matter since the system becomes large enough to encompass the Rossby radius even for gravity waves. However, systems dominated by large advective outflows aloft may still lose less heat to the far field due the reduction in vertical wave propagation. In future studies, outward heat and momentum fluxes due to gravity wave propagation should be addressed. This could be done by considering perturbation temperature and momentum fluxes through the box containing the MCS. Such a box would have to be set up outside the boundary of the contiguous anvil, something that is not often done. As the MCS becomes more balanced, the ratio of latent heating gen-

erated within the system to that escaping to the far field would be reduced.

Acknowledgments. Richard Johnson, Roger Pielke, and V. Chandrasekar were members of the Ph.D. committee that guided this research. Ray McAnelly also provided guidance and was a coinvestigator with the field project. Special thanks goes to the Cotton and Pielke groups, who over the years have worked hard to constantly improve RAMS. Jim Edwards, Bob Walko, and Craig Treback were in charge of RAMS code implementation and improvement through some or all of this time. Jerome Schmidt (NRL) provided the MAPS and mesonet data, while the degribbing software was provided by Greg Thompson (NCAR). Computer and software support were provided by Donna Chester, Doug Burks, John Blanco, and Steve Finley. Brenda Thompson and Abby Hodges helped with the manuscript preparation. This work was supported by the National Science Foundation, under Grants ATM-9118963, ATM-9420045, ATM-9900929, and through a 20-h minigrant from CSU-CHILL Cooperative Agreement ATM-8919080.

REFERENCES

- Anderson, C. J., and R. W. Arritt, 1998: Mesoscale convective complexes and persistent elongated convective systems over the United States during 1992 and 1993. *Mon. Wea. Rev.*, **126**, 578–599.
- Avissar, R., and Y. Mahrer, 1988: Mapping frost-sensitive areas with a three-dimensional local-scale numerical model. Part I: Physical and numerical aspects. *J. Appl. Meteor.*, **27**, 400–413.
- Bartels, D. L., and R. A. Maddox, 1991: Midlevel cyclonic vortices generated by mesoscale convective systems. *Mon. Wea. Rev.*, **119**, 104–118.
- Benjamin, S. G., K. A. Brewster, R. Brümmner, B. F. Jewett, T. W. Schlatter, T. L. Smith, and P. A. Stamus, 1991: An isentropic three-hourly data assimilation system using ACARS aircraft observations. *Mon. Wea. Rev.*, **119**, 888–906.
- Blanchard, D. O., W. R. Cotton, and J. M. Brown, 1998: Mesoscale circulation growth under conditions of weak inertial stability. *Mon. Wea. Rev.*, **126**, 118–140.
- Bluestein, H. B., and M. H. Jain, 1985: Formation of mesoscale lines of precipitation: Severe squall lines in Oklahoma during the spring. *J. Atmos. Sci.*, **42**, 1711–1732.
- Bosart, L. F., and F. Sanders, 1981: The Johnstown flood of July 1977: A long-lived convective system. *J. Atmos. Sci.*, **38**, 1616–1642.
- Bretherton, C. S., and P. K. Smolarkiewicz, 1989: Gravity waves, compensating subsidence, and detrainment around cumulus clouds. *J. Atmos. Sci.*, **46**, 740–759.
- Brown, J. M., 1979: Mesoscale unsaturated downdrafts driven by rainfall evaporation: A numerical study. *J. Atmos. Sci.*, **36**, 313–338.
- Clark, T. L., and R. D. Farley, 1984: Severe downslope windstorm calculations in two and three spatial dimensions using anelastic interactive grid nesting: A possible mechanism for gustiness. *J. Atmos. Sci.*, **41**, 329–350.
- , and W. D. Hall, 1991: Multi-domain simulations of the time dependent Navier–Stokes equations: Benchmark error analysis of some nesting procedures. *J. Comput. Phys.*, **92**, 456–481.
- Cotton, W. R., and R. A. Anthes, 1989: *Storm and Cloud Dynamics*. International Geophysics Series, Vol. 44, Academic Press, 883 pp.
- , M. S. Lin, R. L. McAnelly, and C. J. Treback, 1989: A composite model of mesoscale convective complexes. *Mon. Wea. Rev.*, **117**, 765–783.
- Davies, H. C., 1983: Limitations of some common lateral boundary schemes used in regional NWP models. *Mon. Wea. Rev.*, **111**, 1002–1012.
- Fovell, R., D. R. Durran, and J. R. Holton, 1992: Numerical simulations of convectively generated stratospheric gravity waves. *J. Atmos. Sci.*, **49**, 1427–1442.
- Fritsch, J. M., J. D. Murphy, and J. S. Kain, 1994: Warm core vortex amplification over land. *J. Atmos. Sci.*, **51**, 1780–1807.
- Hill, G. E., 1974: Factors controlling the size and spacing of cumulus clouds as revealed by numerical experiments. *J. Atmos. Sci.*, **31**, 646–673.
- Johnson, R. H., and D. L. Bartels, 1992: Circulations associated with a mature-to-decaying midlatitude mesoscale convective system: Part II: Upper-level features. *Mon. Wea. Rev.*, **120**, 1301–1320.
- , B. D. Miner, and P. E. Ciesielski, 1995: Circulations between mesoscale convective systems along a cold front. *Mon. Wea. Rev.*, **123**, 585–599.
- Kain, J. S., and J. M. Fritsch, 1998: Multiscale convective overturning in mesoscale convective systems: Reconciling observations, simulations and theory. *Mon. Wea. Rev.*, **126**, 2254–2273.
- Klemp, J. B., and R. B. Wilhelmson, 1978a: The simulation of three-dimensional convective storm dynamics. *J. Atmos. Sci.*, **35**, 1070–1096.
- , and —, 1978b: Simulations of right- and left-moving storms produced through storm splitting. *J. Atmos. Sci.*, **35**, 1097–1110.
- Klimowski, B. A., 1994: Initiation and development of rear inflow within the 28–29 June 1989 North Dakota mesoconvective system. *Mon. Wea. Rev.*, **122**, 765–779.
- Knupp, K. R., B. Geerts, and J. D. Tuttle, 1998: Analysis of a small, vigorous mesoscale convective system in a low-shear environment. Part II: Evolution of the stratiform precipitation and mesoscale flows. *Mon. Wea. Rev.*, **126**, 1837–1858.
- Laing, A. G., and J. M. Fritsch, 1997: The global population of mesoscale convective complexes. *Quart. J. Royal Meteor. Soc.*, **123**, 389–405.
- LeMone, M. A., 1983: Momentum transport by a line of cumulonimbus. *J. Atmos. Sci.*, **40**, 1815–1834.
- Lilly, D. K., 1962: On the numerical simulation of buoyant convection. *Tellus*, **XIV**, 148–172.
- Louis, J. F., 1979: A parametric model of vertical eddy fluxes in the atmosphere. *Bound.-Layer Meteor.*, **17**, 187–202.
- Loveland, T. R., J. W. Merchant, D. O. Ohlen, and J. F. Brown, 1991: Development of a land-cover characteristics database for the conterminous U.S. *Photogramm. Eng. Remote Sens.*, **57**, 1453–1463.
- Maddox, R. A., 1980: Mesoscale convective complexes. *Bull. Amer. Meteor. Soc.*, **61**, 1374–1387.
- , 1983: Large-scale meteorological conditions associated with midlatitude, mesoscale convective complexes. *Mon. Wea. Rev.*, **111**, 1475–1493.
- Mahrer, Y., and R. A. Pielke, 1977: A numerical study of the airflow over irregular terrain. *Beitr. Phys. Atmos.*, **50**, 98–113.
- Mapes, B. E., 1993: Gregarious tropical convection. *J. Atmos. Sci.*, **50**, 2026–2037.
- McAnelly, R. L., and W. R. Cotton, 1986: Meso- β -scale characteristics of an episode of meso- α -scale convective complexes. *Mon. Wea. Rev.*, **114**, 1740–1770.
- , J. E. Nachamkin, W. R. Cotton, and M. E. Nicholls, 1997: Upscale evolution of MCSs: Doppler radar analysis and analytical investigation. *Mon. Wea. Rev.*, **125**, 1083–1110.
- Nachamkin, J. E., 1998: Observational and numerical analysis of the genesis of a mesoscale convective system. Ph.D. dissertation, Dept. of Atmospheric Science Paper 643, Colorado State University, 219 pp. [Available from Dept. of Atmospheric Science, Colorado State University, Fort Collins, CO 80523.]
- , and W. Cotton, 1998: Interacting solenoidal circulations and their role in convective orogenesis. Preprints, *Eighth Conf. on*

- Mountain Meteorology*, Flagstaff, AZ, Amer. Meteor. Soc., 297–301.
- , R. L. McAnelly, and W. R. Cotton, 1994: An observational analysis of a developing mesoscale convective complex. *Mon. Wea. Rev.*, **122**, 1168–1188.
- , —, and —, 2000: Interactions between a developing mesoscale convective system and its environment. Part I: Observational analysis. *Mon. Wea. Rev.*, **128**, 1205–1224.
- Nicholls, M. E., R. A. Pielke, and W. R. Cotton, 1991: Thermally forced gravity waves in an atmosphere at rest. *J. Atmos. Sci.*, **48**, 1869–1884.
- Olsson, P. Q., and W. R. Cotton, 1997: Balanced and unbalanced circulations in a primitive equation simulation of a midlatitude MCC. Part II: Analysis of balance. *J. Atmos. Sci.*, **54**, 479–497.
- Pandya, R. D., and D. Durran, 1996: The influence of convectively generated thermal forcing on the mesoscale circulation around squall lines. *J. Atmos. Sci.*, **53**, 2925–2951.
- , —, and C. Bretherton, 1993: Comments on “Thermally forced gravity waves in an atmosphere at rest.” *J. Atmos. Sci.*, **50**, 4097–4101.
- Pielke, R. A., and Coauthors, 1992: A comprehensive meteorological modeling system—RAMS. *Meteor. Atmos. Phys.*, **49**, 69–91.
- Rotunno, R., J. B. Klemp, and M. L. Weisman, 1988: A theory for strong, long-lived squall lines. *J. Atmos. Sci.*, **45**, 463–485.
- Schmidt, J. M., and W. R. Cotton, 1990: Interactions between upper and lower tropospheric gravity waves on squall line structure and maintenance. *J. Atmos. Sci.*, **47**, 1205–1222.
- Smagorinsky, J., 1963: General circulation experiments with the primitive equations. Part I: The basic experiment. *Mon. Wea. Rev.*, **91**, 99–164.
- Smull, B. F., and R. A. Houze Jr., 1987: Rear inflow in squall lines with trailing stratiform precipitation. *Mon. Wea. Rev.*, **115**, 2869–2889.
- Szoke, E. J., M. L. Weisman, J. M. Brown, F. Caracena, and T. W. Schlatter, 1984: A subsynoptic analysis of the Denver tornado of 3 June 1981. *Mon. Wea. Rev.*, **112**, 790–808.
- Tremback, C. J., and R. Kessler, 1985: A surface temperature and moisture parameterization for use in mesoscale numerical models. Preprints, *Seventh Conf. on Numerical Weather Prediction*, Montreal, PQ, Canada, Amer. Meteor. Soc., 433–434.
- Tripoli, G., and W. R. Cotton, 1989: A numerical study of an observed orogenic mesoscale convective system. Part I: Simulated genesis and comparison with observations. *Mon. Wea. Rev.*, **117**, 273–304.
- Velasco, I., and J. M. Fritsch, 1987: Mesoscale convective complexes in the Americas. *J. Geophys. Res.*, **92**, 9591–9613.
- Walko, R., W. R. Cotton, M. P. Meyers, and J. Y. Harrington, 1995: New RAMS cloud microphysics parameterization. Part I: The single-moment scheme. *Atmos. Res.*, **38**, 29–62.
- Wetzel, P. J., and J. T. Chang, 1988: Evapotranspiration from non-uniform surfaces: A first approach for short-term numerical weather prediction. *Mon. Wea. Rev.*, **116**, 600–621.
- Yuter, S. E., and R. A. Houze Jr., 1995a: Three-dimensional kinematic and microphysical evolution of Florida cumulonimbus. Part I: Spatial distribution of updrafts, downdrafts, and precipitation. *Mon. Wea. Rev.*, **123**, 1921–1940.
- , and —, 1995b: Three-dimensional kinematic and microphysical evolution of Florida cumulonimbus. Part II: Frequency distributions of vertical velocity, reflectivity, and differential reflectivity. *Mon. Wea. Rev.*, **123**, 1941–1963.
- , and —, 1995c: Three-dimensional kinematic and microphysical evolution of Florida cumulonimbus. Part III: Vertical mass transport, mass divergence, and synthesis. *Mon. Wea. Rev.*, **123**, 1964–1983.